JACS
JOURNAL OF THE AMERICAN CHEMICAL SOCIETY
Article
pubs.acs.org/JACS

All-Polymer Solar Cell Performance Optimized via Systematic Molecular Weight Tuning of Both Donor and Acceptor Polymers

Nanjia Zhou,[†] Alexander S. Dudnik,[‡] Ting I. N. G. Li,[†] Eric F. Manley,[‡,⊥] Thomas J. Aldrich,[‡] Peijun Guo,[†] Hsueh-Chung Liao,[‡] Zhihua Chen,[§] Lin X. Chen,*[,‡,⊥] Robert P. H. Chang,*[,†] Antonio Facchetti,*[,‡,§] Monica Olvera de la Cruz,*[,†] and Tobin J. Marks*[,†,‡]

[†]Department of Materials Science and Engineering and the Argonne Northwestern Solar Energy Research Center (ANSER) and [‡]Department of Chemistry and the Materials Research Center, Northwestern University, 2145 Sheridan Road, Evanston, Illinois 60208, United States

[§]Polyera Corporation, 8045 Lamon Avenue, Skokie, Illinois 60077, United States

[⊥]Chemical Sciences and Engineering Division, Argonne National Laboratory, 9700 South Cass Avenue, Lemont, Illinois 60439, United States

Supporting Information

ABSTRACT: The influence of the number-average molecular weight (M_n) on the blend film morphology and photovoltaic performance of all-polymer solar cells (APSCs) fabricated with the donor polymer poly[5-(2-hexyldodecyl)-1,3-thieno[3,4-*c*]pyrrole-4,6-dione-*alt*-5,5-(2,5-bis(3-dodecylthiophen-2-yl)-thiophene)] (**PTPD3T**) and acceptor polymer poly{[*N*,*N*′-bis(2-octyldodecyl)naphthalene-1,4,5,8-bis(dicarboximide)-2,6-diyl]-*alt*-5,5′-(2,2′-bithiophene)} (P(NDI2OD-T2); **N2200**) is systematically investigated. The M_n effect analysis of *both* **PTPD3T** and **N2200** is enabled by implementing a polymerization strategy which produces conjugated polymers with tunable M_ns. Experimental and coarse-grain modeling results reveal that systematic M_n variation greatly influences both intrachain and interchain interactions and ultimately the degree of phase separation and morphology evolution. Specifically, increasing M_n for both polymers shrinks blend film domain sizes and enhances donor−acceptor polymer−polymer interfacial areas, affording increased short-circuit current densities (J_{sc}). However, the greater disorder and intermixed feature proliferation accompanying increasing M_n promotes charge carrier recombination, reducing cell fill factors (*FF*). The optimized photoactive layers exhibit well-balanced exciton dissociation and charge transport characteristics, ultimately providing solar cells with a 2-fold PCE enhancement versus devices with nonoptimal M_ns. Overall, it is shown that proper and precise tuning of both donor and acceptor polymer M_ns is critical for optimizing APSC performance. In contrast to reports where maximum power conversion efficiencies (PCEs) are achieved for the highest M_ns, the present two-dimensional M_n optimization matrix strategy locates a PCE "sweet spot" at intermediate M_ns of both donor and acceptor polymers. This study provides synthetic methodologies to predictably access conjugated polymers with desired M_n and highlights the importance of optimizing M_n for *both* polymer components to realize the full potential of APSC performance.

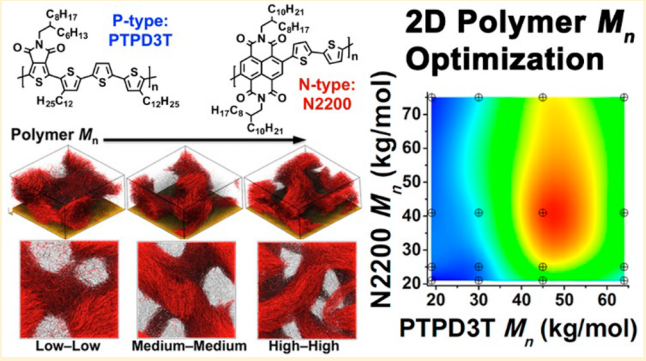

INTRODUCTION

Extensive research efforts by the soft matter solar cell community have afforded rapid advances in the performance of polymer solar cells (PSCs).[1−7] Using conventional fullerene-based acceptors, the rational design of polymer donor structures with proper frontier molecular orbital (FMO) energies and band gaps as well as substituents and processing have yielded significant breakthroughs in PSC power conversion efficiencies (PCEs), now exceeding 11%.[3,8] Despite the success of the fullerene acceptors, they suffer from several limitations which significantly constrain the development of new donor materials; these include limited optical absorption, costly production, and fixed band alignment.[9−19] Therefore, recent studies have focused on developing and understanding alternative acceptors.[20−27] Among these candidates, π-conjugated electron-transporting polymers have been investigated and achieved excellent PCEs > 7.5%.[14,16,28] Relative to the extensively studied polymer:fullerene cells, all-polymer solar cells (APSCs) based on the all-polymer donor−acceptor photoactive layers offer unique attractions to tune and match chemical and electronic properties of the blend components and to explore very different film morphologies arising from the unique mixing characteristics of the macromolecular constitu-

Received: October 14, 2015
Published: December 31, 2015

DOI: 10.1021/jacs.5b10735
J. Am. Chem. Soc. 2016, 138, 1240−1251

Scheme 1. Macromolecular Structures and Device Architecture of APSCs Based on Active Layer Blends of PTPD3T and N2200

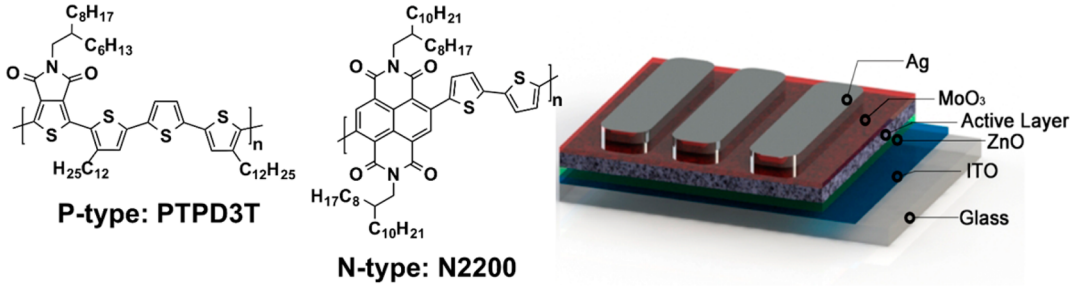

ents. Thus, this blend architecture should provide new opportunities for further enhancing PSC device metrics, particularly by increasing the open-circuit voltage (V_{oc}) and the short-circuit current density (J_{sc}), as well as morphological stability to thermal and mechanical stress.[29]

It is well known that the number-average molecular weight (M_n) of a polymer has a profound influence on macromolecular ordering and microstructure and additionally on optoelectronic and charge transport characteristics, thus making it one of the key parameters governing the performance of fullerene-based solar cells.[30−36] In such devices, donor polymers with higher M_ns typically have higher degrees of ordering, resulting in enhanced light absorption and hole mobility, which contribute to higher J_{sc} and *FF* parameters, ultimately enhancing PCE.

APSCs have historically lagged behind polymer:fullerene PSCs in performance metrics, principally due to energetically favored polymer−polymer demixing,[37] which results in large-scale phase separation, limiting exciton diffusion and current output.[38] While controlling film processing parameters to improve film morphology is a promising strategy,[11,27,39] such approaches are highly empirical and system dependent, often providing limited performance benefits. In contrast, systematically tuning APSC component polymer M_ns should in principle provide a more general device optimization strategy. To date, this approach has received only limited attention, with the highest PCEs achieved with the donor polymers having the highest accessible polymer M_n values.[15] However, to the best of our knowledge, M_n effects have been explored only for one of the two component polymers, while the M_n of the second component was held constant. Note also that rational selection of both donor and acceptor polymer M_ns has been elusive, mainly due to a poor understanding of polymer M_n effects on the resulting blend physical properties, polymer−polymer interactions, and blend phase separation.[31,40] Thus, guides to the simultaneous tuning of both donor and acceptor M_ns have yet to be established.

In this study, we simultaneously investigate the influence of the M_n values of *both* donor and acceptor polymers on the active layer film morphology, photophysics, and performance metrics of solar cells fabricated with a high-performance polymer−polymer blend system. From previous work, the high-performance polymer poly[5-(2-hexyldodecyl)-1,3-thieno-[3,4-*c*]pyrrole-4,6-dione-*alt*-5,5-(2,5-bis(3-dodecylthiophen-2-yl)thiophene)] (**PTPD3T**) was selected as the donor semiconductor and poly{[*N*,*N*′-bis(2-octyldodecyl)-naphthalene-1,4,5,8-bis(dicarboximide)-2,6-diyl]-*alt*-5,5′-(2,2′-bithiophene)} (P(NDI2OD-T2), **N2200**) as the acceptor semiconductor (Scheme 1). **N2200** has been widely used in APSCs (PCEs up to 5.7%),[11] and such polymers are the best-performing acceptor polymers discovered to date (PCEs up to 7.7%).[41] Broad control of the component polymer M_ns is accomplished here via a straightforward synthetic strategy based on the Carothers equation, taking into account the comonomer ratios and extent of polymerization. The product polymers are characterized by an array of techniques, including high-temperature GPC, optical spectroscopy, cyclic voltammetry (CV), ultraviolet photoelectron spectroscopy (UPS), and differential scanning calorimetry (DSC). In addition, the APSC blends are characterized by transmission electron microscopy (TEM), grazing incidence wide-angle X-ray scattering (GIWAXS), space charge limited current (SCLC) mobility, photovoltaic response, and variable light intensity measurements. The results show that increasing both donor and acceptor polymer M_n results in higher degrees of polymer mixing in the blends. This effect is reflected in inverted architecture APSC performance, where PCEs vary by as much as 2-fold for devices based on different M_n polymer combinations. The observed trends are in good agreement with the charge transport and light intensity studies and reveal a performance "sweet spot" at intermediate M_ns. Finally, a universal coarse-grained model simulation of the blend morphology provides valuable insights into physical processes that occur during blend film formation and support the experimental findings. The results obtained in this work reveal important optoelectronic properties in all-polymer blends and establish a general strategy for APSC efficiency optimization.

RESULTS AND DISCUSSION

Synthesis of Polymers with Predictable Molecular Weights and Polymer Characterization. The conventional preparation of semiconducting π-conjugated in-chain donor−acceptor polymers with variable M_n has typically relied on fractionation of the crude polycondensation product using either Soxhlet extraction and preparative gel permeation chromatography (GPC)[42−46] or comonomer ratio variation.[47,48] Although these approaches are relatively straightforward, they do not provide precise control of product polymer M_n. A more effective strategy to achieve controllable polymer M_ns for polycondensation reactions is to vary the stoichiometric ratio r between reactant monomers[35,49] according to a simplified Carothers model (eq 1), where M_0 is the repeat unit molecular weight and N_{AA} and N_{BB} are quantities of bifunctional monomers AA and BB, respectively.[50,51] Equation 1 can be derived from the standard Carothers equation (eq 2) assuming complete (100%) limiting monomer conversion (p = 1.0).[50,52]

$$M_n = M_0\frac{(1+r)}{(1-r)};\ \text{where } r = \frac{N_{AA}}{N_{BB}} \le 1 \qquad (1)$$

DOI: 10.1021/jacs.5b10735
J. Am. Chem. Soc. 2016, 138, 1240−1251

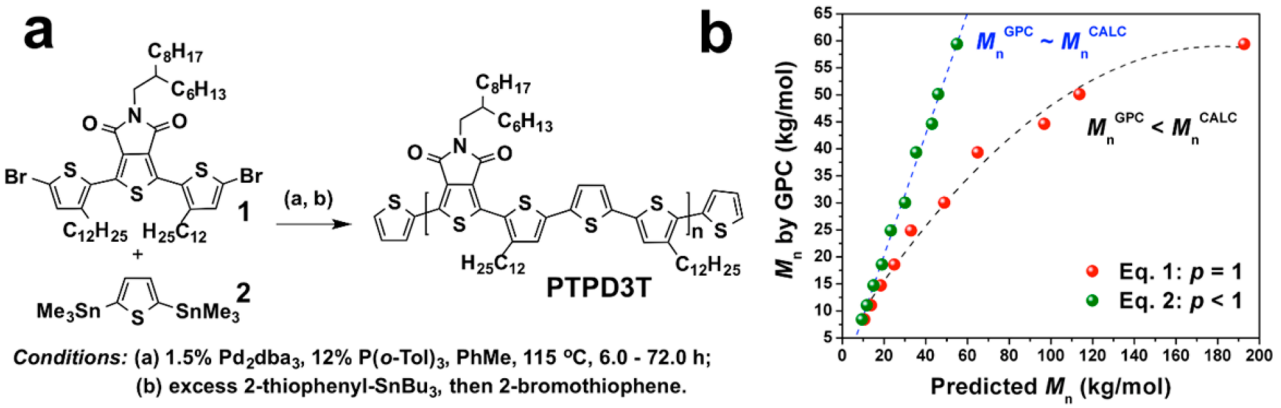

Figure 1. Synthesis of **PTPD3T** polymers with predictable number-average molecular weights, M_ns. (a) Synthetic route to **PTPD3T** polymers including structures of the comonomers **1** and **2** and the polymerization reaction conditions. (b) Correlation between **PTPD3T** M_ns predicted using eqs 1 (p = 1, red dots) and 2 (p < 1, green dots) versus those obtained from GPC analysis.

Table 1. Molecular Weight and Optoelectronic Properties of PTPD3T Polymers

polymer batch	excess **1** (%)[a]	M_n (kg/mol)[d]	PDI[d]	λ_{max} (nm)[e]	E_g^{opt} (eV)[g]	HOMO (eV)[h]	LUMO (eV)[i]
8P	20	8.4	1.57	488, 582,[f] 631[f]	1.84	−5.21	−3.37
11P	15	11.0	1.96	490, 582,[f] 630[f]	1.85	−5.20	−3.35
15P	11	14.7	1.67	496, 580, 629[f]	1.84	−5.24	−3.40
19P	8	18.6	1.89	506, 582, 630[f]	1.84	−5.31	−3.47
25P	6	24.9	1.55	522, 582, 629[f]	1.85	−5.27	−3.42
30P	4	30.1	1.75	582, 629[f]	1.85	−5.26	−3.41
39P	3	39.3	2.16	580, 629[f]	1.84	−5.29	−3.45
45P	2	44.6	2.02	583, 630[f]	1.84	−5.30	−3.46
50P	1.7	50.1	2.18	582, 629[f]	1.86	−5.29	−3.43
59P	1	59.4	1.98	583, 629[f]	1.85	−5.28	−3.43
62P	0	61.8	1.87	582, 630[f]	1.86	−5.27	−3.41
64P	0[b]	64.5	1.87	582, 630[f]	1.85	−5.27	−3.42
67P	0[c]	67.0	1.86	581, 630[f]	1.84	−5.29	−3.45

[a]Unless otherwise noted, all polymerizations performed for 6 h. [b]Polymerization performed for 24 h. [c]Polymerization performed for 72 h. [d]Determined by GPC at 150 °C in 1,2,4-trichlorobenzene. [e]Solution absorption spectra (0.015 mg/mL in $CHCl_3$). [f]Shoulder. [g]Optical gap estimated from absorption edge of as-cast thin film (5 mg/mL $CHCl_3$ solution). [h]Determined by UV photoemission spectroscopy (UPS) (see SI). [i]Calculated according to $E_{LUMO} = E_g^{opt} + E_{HOMO}$.

$$M_n = M_0\frac{(1+r)}{(1+r-2rp)};\ \text{where } p \le 1 \quad (2)$$

For the synthesis of **PTPD3T** polymers (Figure 1a),[6] it is found that the conversion p is <1 since the M_ns calculated from eq 1 are significantly greater than those obtained by GPC,[34] indicating that the predictable control over M_ns following eq 1 is limited (see also Table S1 and Figure S2 in the SI). Thus, to synthesize **PTPD3T** polymers with predictable M_ns, eq 2 which takes into account incomplete conversion of a limiting monomer (p < 1.0) was employed as a guide. The key assumption here is that p remains constant for fixed concentration, time, catalyst loading, and temperature, and where mass-transfer issues are negligible. Since transmetalation is typically the rate-determining step in Stille reactions,[53,54] we varied the amounts of comonomer **1** to maintain the concentration and conversion (p) of distannane **2** constant (Figure 1a). Comonomer reagents **1** and **2** were rigorously purified, and all polymerization reactions were performed using stock solutions of Pd/ligand precatalyst components and carefully weighed reactants (±0.01 mg) to ensure reproducibility. To estimate the conversion value p, the polymerization was performed in the presence of 4.0 mol % excess comonomer **1**, affording **PTPD3T** with M_n = 30.1 kg/mol by high-temperature GPC (a batch abbreviated hereafter as **30P**; where the number indicates the rounded M_n and **P** denotes p-type donor polymer). According to eq 3 this corresponds to the value of p = 0.9875 (stoichiometric ratio r = 0.9615; Table 1).

$$p = \frac{(M_n - M_0)(1+r)}{2M_n r} \quad (3)$$

Next, using polymerization conditions that conformed to the constraints of eq 2, specifically 6 h reaction time, $p \approx 0.9875$ for a broad r < 1 range, yielded **PTPD3T**s with M_ns ranging from ∼8 to ∼59 kg/mol (**8P**−**59P**; Table 1). The excellent linear correlation (r^2 = 0.996) between calculated M_ns (M_n^{CALC}) and those determined by GPC (M_n^{GPC}) corroborates the control over **PTPD3T** M_ns when eq 2 is followed (Figure 1b, green dots and blue line). This correlation exhibits a far better fit to the experimental GPC data than that based on eq 1 (Figure 1b, red dots and black line), where much higher M_ns would be expected (see also SI Table S1). Note also a growing disparity between the M_n values predicted by the two different synthetic approaches as the monomer imbalance decreases. Finally, **PTPD3T** batches with even higher M_ns ≈ 62, 64, and 67 kg/mol (**62P**, **64P**, and **67P**) were prepared using the stoichiometric ratio of comonomers (r = 1.00) and extending the reaction time from 6 to 24 and 72 h, respectively (Table 1

DOI: 10.1021/jacs.5b10735
J. Am. Chem. Soc. 2016, 138, 1240−1251

and S1). Note here that the M_ns predicted with eq 2 for the stoichiometric cases deviate from the experimental results, likely due to problematic mass-transfer effects at higher polymer M_ns and viscosities.[55]

The n-type polymer **N2200**[56−59] batches with M_ns in the 21−75 kg/mol range (**21N**−**75N**) were obtained from Polyera Corp. In Table 2, **N** specifies n-type **N2200** polymer, with the preceding number denoting the M_n in kg/mol rounded to the nearest one.

Table 2. Molecular Weight and Optoelectronic Properties of N2200 Polymers

polymer batch	M_n (kg/mol)[a]	PDI[a]	λ_{max} (nm)[b]	E_g^{opt} (eV)[c]	HOMO (eV)[d]	LUMO (eV)[e]
21N	20.7	2.70	385, 679	1.46	−5.37	−3.91
25N	25.1	2.98	386, 665	1.47	−5.38	−3.91
41N	41.0	2.48	387, 698	1.47	−5.38	−3.91
75N	74.8	2.25	389, 701	1.46	−5.37	−3.91

[a]Determined by GPC at 150 °C in 1,2,4-trichlorobenzene. [b]Solution absorption spectra (0.02 mg/mL in $CHCl_3$). [c]Optical energy gap estimated from absorption edge of the as-cast thin film (5 mg/mL $CHCl_3$ solution). [d]Calculated according to $E_{HOMO} = E_{LUMO} - E_g^{opt}$. [e]Electrochemically determined vs Fc/Fc^+; $E_{LUMO} = -(E_{red}^{onset} + 4.88)$.

Polymer Optoelectronic and Thermal Properties. The optical properties of the **PTPD3T** and **N2200** polymer batches were investigated by optical absorption spectroscopy both as thin films and in solution (Figure 2a and 2b). Data are summarized in Tables 1 and 2. Figure 2a and 2b indicates that the solution absorption spectra exhibit a clear dependence on the **PTPD3T** and **N2200** M_ns, with the higher-M_n polymers showing red-shifted absorption maxima (λ_{max}) presumably reflecting increased π-conjugation lengths and chain aggregation.[60−62] Interestingly, larger solution-phase λ_{max} variations are observed for **PTPD3T** than for **N2200**. Specifically, lower-M_n **PTPD3T**s (**8P**−**25P**) exhibit three absorption features with λ_{max} values ranging from 488 to 522 nm and two shoulders located at ∼580 and ∼630 nm. The former feature red shifts gradually, becomes a shoulder in **30P**−**39P**, and then disappears in higher-M_n polymers, while the latter two features gradually increase in intensity with increasing polymer M_n and evolve into the absorption maxima and shoulder (580−583 nm, 629−630 nm) of the higher molecular weight **PTPD3T** samples. In contrast, the thin film optical spectra of both **PTPD3T** and **N2200** exhibit minimal M_n dependence (**PTPD3T**: $\lambda_{max} \approx$ 571−578 and $\lambda_{shoulder} \approx$ 612−618 nm; **N2200**: λ_{max1} = 392 and $\lambda_{max2} \approx$ 696−701 nm). Going from the solution to film spectra, high-M_n **PTPD3T** (>**45P**) and **N2200** (>**41N**) batches exhibit minimal differences in optical absorption profiles, suggesting extensive aggregation in solution for M_n > 40 kg/mol. Note that despite being visually transparent to the eye, the **PTPD3T** solutions in chloroform exhibit a certain degree of preaggregation, as evidenced by a dark blue/purple to orange color change upon raising the temperature. The sharp vibronic features in the **PTPD3T** spectra imply ordered solid-state structures.[63,64] The optical band gaps (E_g^{opt}) of the **PTPD3T** and **N2200** batches, calculated from the film absorption onsets, are nearly identical within each polymer series, ∼1.84−1.86 eV for **PTPD3T** (Table 1) and ∼1.46−1.47 eV for **N2200** (Table 2).

The UPS-derived HOMO energies of the **PTPD3T**s lie from ∼−5.28 to −5.22 eV and display little variation for the range of M_ns (8−67 kg/mol) investigated in this study. The **PTPD3T**

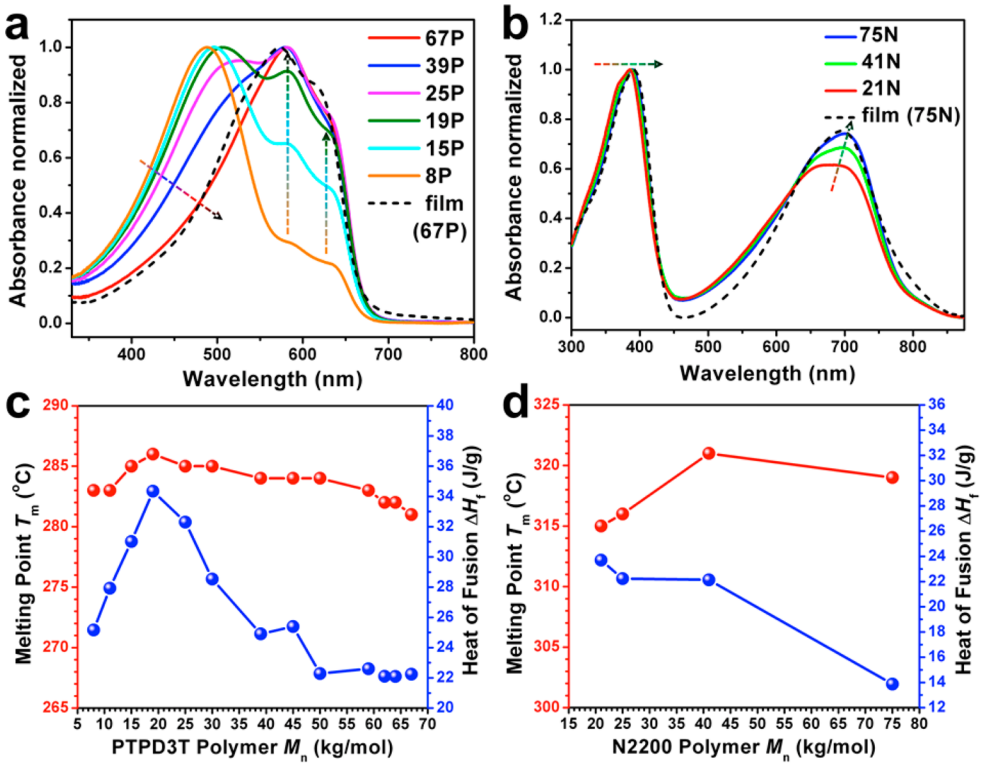

Figure 2. Optical absorption spectra of (a) **PTPD3T** polymers in chloroform solution (0.015 mg/mL) and (b) **N2200** polymers in chloroform solution (0.02 mg/mL), as a function of polymer M_n. Representative thin film absorption spectra for **PTPD3T** (**67P**) and **N2200** (**75N**) are included as dashed lines. Thermal properties of (c) **PTPD3T** and (d) **N2200** polymers as a function of polymer M_n.

DOI: 10.1021/jacs.5b10735
J. Am. Chem. Soc. 2016, 138, 1240−1251

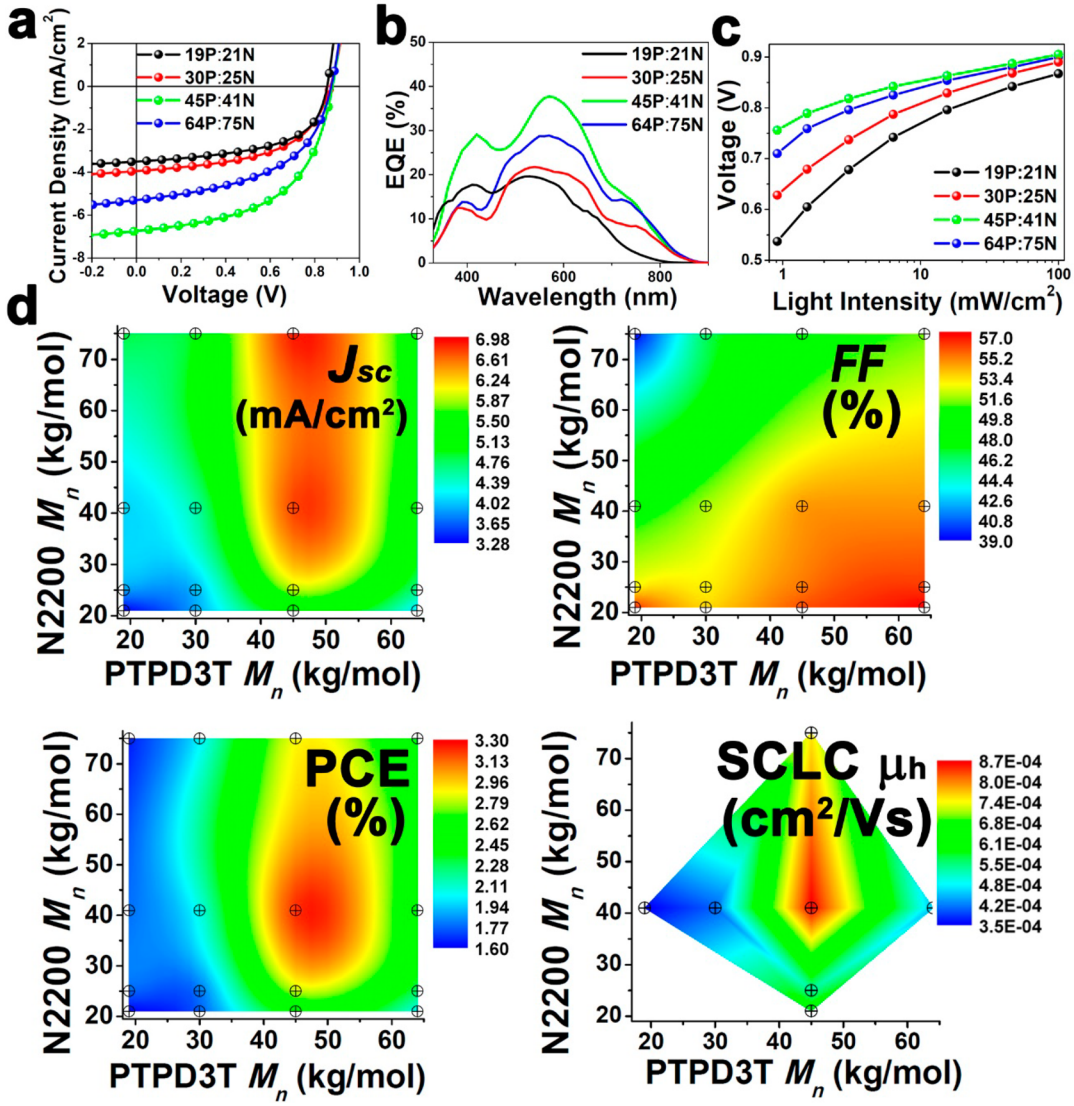

Figure 3. APSC device metrics. (a) $J-V$ and (b) EQE characteristics. (c) Light intensity dependence of V_{oc} for all-polymer devices based on **19P**:**21N**, **30P**:**25N**, **45P**:**41N**, and **64P**:**75N** blends. (d) Contour color-filled comparative maps of J_{sc}, *FF*, and PCE for APSCs in the 4 × 4 M_n matrix. SCLC hole mobilities (μ_h) for "horizontal" (i.e., varying **PTPD3T** M_n from 19 to 64 kg/mol) and "vertical" matrix directions (i.e., varying **N2200** M_n from 21 to 75 kg/mol) are also presented.

LUMO energies compiled in Table 1 are derived from the film optical band gaps (E_g^{opt}) and HOMO levels, and are in the range from −3.35 to −3.47 eV. The UPS/E_g^{opt}-derived HOMO and LUMO energies of the **N2200** batches are −5.90 and −4.30 eV, respectively, yielding sufficiently large LUMO−LUMO and HOMO−HOMO offsets, to ensure efficient exciton dissociation.[65,66] The cyclic voltammetry-derived HOMO and LUMO energies of **PTPD3T** (Table S5) and **N2200** (Table 2) not unexpectedly deviate within a reasonable margin from the UPS data[67,68] but remain fairly constant with the variations in the polymer M_ns.

Polymer thermal properties were investigated using differential scanning calorimetry (DSC) (Figure 2c and 2d). **PTPD3T** batches **8P**−**67P** have melting points within a fairly narrow range of 283−286 °C (T_m) and exhibit two close but discrete endotherms[6,69] and one exotherm with peak maxima at ∼261−268 °C (T_{mp1}), ∼269−277 °C (T_{mp2}), and ∼238−250 °C (T_{cp}) (Figure S8, SI), thus indicating some degree of crystallinity for these polymers.[6] The melting points, T_m, of the **PTPD3T** series, the highest temperature points on the melting endotherms,[37] and the enthalpies of fusion, ΔH_f, increase with increasing M_n from the lowest molecular weight **8P** and reach maxima at 286 °C and 34.4 J/g, respectively, for **19P** (Figure 2c), which is attributable to enhanced crystallinity.[70,71] However, further increases in M_n from **19P** to **67P** lead to a gradual decrease of T_m to 281 °C and a relatively sharp decline of ΔH_f to ∼22 J/g (Figure 2c), likely reflecting a synchronous increase in viscosity and polymer chain entanglement during melting.[70] Collectively, the above data indicate that the highest degree of crystallinity is reached for **PTPD3T** batches with intermediate molecular weights (**15P**−**25P**),[70] while the lowest crystallinity is achieved for very high molecular weight polymers (**50P**−**67P**).

The **N2200** polymers have two thermal transitions at 306−317 °C (endo, T_{mp}) and 279−295 °C (exo, T_{cp}) (Figure 2d). By increasing the M_n from **21N** to **41N** T_m increases from 315 to 321 °C, while the highest M_n batch **75N** exhibits a slightly lower T_m (319 °C). In contrast to **PTPD3T** and in accord with previous reports,[56] the highest ΔH_f and crystallinity are observed for the lowest **21N** molecular weights (Figure 2d),

DOI: 10.1021/jacs.5b10735
J. Am. Chem. Soc. 2016, 138, 1240−1251

which can be explained by reduced polymer chain entanglement, resulting in enhanced $\pi-\pi$ stacking interactions. On the basis of the above data, maximum polymer−polymer mixing is expected for the less crystalline, higher-M_n polymers. This result is confirmed both experimentally and in computational studies (vide infra).

Polymer Solar Cell and Charge Transport Characteristics. Four **PTPD3T** donor (**19P**, 19 kg/mol; **30P**, 30 kg/mol; **45P**, 45 kg/mol; **64P**, 64 kg/mol) and four **N2200** acceptor (**21N**, 21 kg/mol; **25N**, 25 kg/mol; **41N**, 41 kg/mol; **75N**, 75 kg/mol) polymer samples, covering a broad range of molecular weights, were selected for study via a 4 × 4 APSC characterization/performance optimization matrix. These APSCs were fabricated using an inverted architecture,[20,72] specifically, ITO/ZnO/active layer/MoO_3/Ag (see more details in the Experimental Section). All active layers were optimized to be ∼70 nm thick, which also allows direct comparison across a wide range of polymer M_ns. Figure 3 and Table 3 summarize the OPV performance metrics as a function of donor and acceptor polymer M_n.

Table 3. Comparison of All-Polymer Solar Cell Device Metrics with Varying Number-Average Molecular Weights of PTPD3T and N2200

PTPD3T M_n (kg/mol)	N2200 M_n (kg/mol)	V_{oc} (V)	J_{sc} (mA/cm^2)	FF (%)	PCE (%)
19	21	0.86	3.29	56.8	1.61
	25	0.87	3.85	52.9	1.77
	41	0.88	4.06	50.2	1.79
	75	0.88	4.83	39.1	1.66
30	21	0.85	3.88	53.5	1.76
	25	0.86	3.93	53.1	1.79
	41	0.88	4.51	51.8	2.06
	75	0.87	4.96	46.5	2.01
45	21	0.85	5.14	56.1	2.45
	25	0.86	5.86	55.3	2.79
	41	0.87	6.75	54.8	3.22
	75	0.84	6.89	49.6	2.87
64	21	0.86	4.15	57.5	2.05
	25	0.87	4.62	56.4	2.27
	41	0.88	5.03	54.8	2.43
	75	0.88	5.28	51.2	2.38

Comparison of the APSC metrics obtained for all possible combinations of donor and acceptor polymer M_ns reveals dramatic variations in PCE, ranging from 1.61% (**19P** + **21N**) to 3.22% (**45P** + **41N**). Note also that all devices display nearly identical V_{oc}s ≈ 0.84−0.88 V, consistent with the observed similarity between polymer FMO energies (Tables 1 and 2); thus, the observed M_n effects on APSC performance are not due to differences in polymer−polymer FMO alignments. The observed J_{sc} and *FF* trends indicate a substantial dependence on the M_ns of both polymers. These trends are exemplified by comparing J_{sc} and EQE of the "diagonal" series (**19P:21N**, **30P:25N**, **45P:41N**, and **64P:75N**) (Figure 3a and 3b).

From photophysical studies, we observe a strong dependence of the V_{oc}s on incident light intensity in this four device series (Figure 3c). The lowest molecular weight polymer blend (**19P:21N**) has the strongest dependence of V_{oc} on light intensity, and this dependence lessens with increasing polymer M_n, reaching the weakest correlation for the **45P:41N** blend. Note also that the highest APSC performance is obtained for this blend. Finally, the light intensity dependence increases again for the highest M_n blend (**64P:75N**). These data clearly indicate that carrier recombination in the APSC active layer blends is strongly dependent on the M_ns of both component polymers. For the best-performing APSCs, the observed weakest dependence of V_{oc} on light intensity suggests a closer-to-ideal diode-type behavior and with bimolecular recombination as the dominant recombination mechanism,[20] whereas in the other blends, recombination mechanisms other than bimolecular (i.e., tail-state and trap-assisted) are operative.[73,74]

From the performance of the 4 × 4 device matrix (Table 3, Figure 3d), it can be seen for a given **PTPD3T** sample that J_{sc} monotonically increases with increasing **N2200** M_n while the *FF* falls. For example, using **19P** as the donor and increasing **N2200** M_n from 21 to 75 kg/mol results in a gradual increase of J_{sc} from 3.29 to 4.83 mA/cm^2, while the *FF* falls from 56.8% to 39.1%, implying a higher degree of recombination for the **75N**-based cells. Thus, concerning PCE, the observed increase in J_{sc} is counterbalanced by the concomitant decline in *FF*. Slightly different trends are observed for **PTPD3T** M_n variations (Figure 3d). Specifically, both J_{sc} and *FF* parameters rise with increasing M_n from 19 to 45 kg/mol. Increasing M_n further to **64P** leads to marginally enhanced *FF*s; however, the J_{sc} values decline sharply. Interestingly, the optimal "sweet-spot" device metrics are achieved in blends of medium-M_n polymers **45P** and **41N** (Figure 3d). Note also that in the case of **45P**, variation of **N2200** M_n increases J_{sc} from 5.14 to 6.89 mA/cm^2 but depresses *FF* from 56.1% to 49.6% (Figure 3d).

Space-charge limited current (SCLC) measurements are important probes of charge transport in the direction perpendicular to the substrate.[75] Here both hole and electron mobilities were investigated in the polymer blends by first varying **N2200** M_n (**45P:21N**, **45P:25N**, **45P:41N**, and **45P:75N**) and then by varying **PTPD3T** M_n (**19P:41N**, **30P:41N**, **45P:41N**, and **64P:41N**) (Table S7). Note that increasing the M_n of **N2200** results in a large monotonic increase of the SCLC electron mobility (μ_e) from 5.2 × 10^{-4} to 1.1 × 10^{-2} cm^2/(V s). However, with increasing **PTPD3T** M_n, the SCLC hole mobility (μ_h) increases from 3.5 × 10^{-4} cm^2/(V s) in **19P:41N** to its peak value of 8.7 × 10^{-4} cm^2/(V s) in **45P:41N** and then declines in **64P:41N**. In agreement with the DSC results discussed above (Figure 2c and 2d), an increasing degree of chain entanglement is expected to hinder $\pi-\pi$ stack ordering and to promote charge trapping in intermolecular charge transport, thus reducing SCLC hole mobilities for the blends employing high-M_n polymers (Figure 3d). Since well-balanced hole and electron carrier transport can reduce the buildup of space charges and positively contribute to APSC *FF*s,[11] note that the increase in **N2200** M_n leads to greater discrepancies between μ_h versus μ_e and thus agrees well with the observed fall in *FF*s in this series.[15,76] Additionally, when using **41N** while varying **PTPD3T** M_n, the best-performing APSC combination (**45P:41N**) again exhibits relatively balanced μ_h and μ_e and the highest *FF*. Overall, the above data demonstrate that polymer blend charge transport characteristics can be optimized using the proper combination of polymer M_ns.

Polymer−Polymer Blend Film Morphology. To better understand all-polymer blend optoelectronic properties, active layer morphologies were investigated using TEM. Figure 4 shows the top-down TEM images of the polymer−polymer blend film 4 × 4 matrix. All image sizes are 500 nm × 500 nm.

DOI: 10.1021/jacs.5b10735
J. Am. Chem. Soc. 2016, 138, 1240−1251

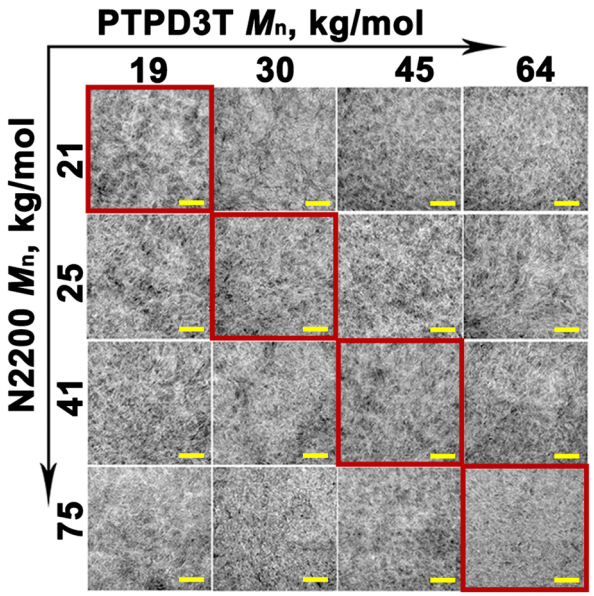

Figure 4. TEM images of the 4 × 4 matrix of all-polymer blend morphologies for different M_n **PTPD3T** and **N2200** polymers. Diagonal direction TEMs are highlighted in red. Scale bars are 100 nm.

Despite a relatively weak contrast between the two polymers, scanning TEM images in both horizontal (i.e., varying **PTPD3T** M_n from 19 to 64 kg/mol) and vertical matrix directions (i.e., varying **N2200** M_n from 21 to 75 kg/mol) reveals a reduction in domain sizes and polymer crystallinities. Note that in the case of thin films employing lower M_n **N2200**, a combination of both short-chain polymers and some fraction of long-chain polymers are present, as indicated by the PDI values (Table 2). Focusing on the diagonal direction and starting from the lowest M_ns of both polymers (**19P:21N**), the TEM images exhibit strongly phase-separated regions with clearly defined, large fibril-like polymer microstructures. Such morphologies are known to introduce large grain boundaries with poorly connected polymer networks, suppressing charge carrier transport.[6,77,78] For medium M_ns of both polymers (**45P:41N**), the film morphologies begin to exhibit more intermixed features, which should enable more efficient exciton scission, all other factors being equal. This is accompanied by relatively continuous polymer domains, which can be critical for efficient charge transport. Finally, using the highest M_n polymers (**64P:75N**), the blend films display the most intermixed and highly disordered characteristics, with the semicrystalline polymer domains the least discernible.

Since TEM has limitations in resolving the differences between blended polymers, grazing incidence wide-angle X-ray scattering (GIWAXS) measurements were also employed. Note that GIWAXS can closely define morphological properties such as domain size and local crystallinity and thus is highly informative for examining blend polymer molecular weight effects. Selected 2D GIWAXS images of the spun-cast blend films on Si/SiO_2 substrates examining the blends **19P:21N**, **30P:25N**, **45P:41N**, and **64P:75N**; hence simultaneous, diagonal M_n variation for both polymers, are shown in Figure 5a. The spectra for other combinations (vertical and horizontal p- or n-type polymer M_n variations) and neat films of **30P**, **65P**, **41N**, and **75N** are provided in Figure S10. All blend films were examined with identical exposure times at an incidence angle of 0.18°. Since neat **PTPD3T** exhibits preferential π-face-on domain orientation while **N2200** exhibits a preference for edge-on domains (Figures 5b–e), it is possible to view d spacings and correlation lengths dominated by each of the separate species in the blend films by examining the (100) peaks of the different orientations separately. While the blend peaks are shifted in comparison to their neat counterparts due to some isotropy in blend domains, the line cut analysis demonstrates that the in-plane (100) peak is closer to the neat **PTPD3T** (100) peak, while the out-of-plane (100) peak is more similar to the **N2200** (100) peak. This is shown in Figure S12. The d spacings are derived from the peak position and correlation lengths calculated using a modified Scherrer analysis.[79] With the films examined, there are three specific groups yielding different trends. First, there is the diagonal group where the molecular weights of both polymers in each film are increased, going from low–low **19P:21N** to high–high **64P:75N**

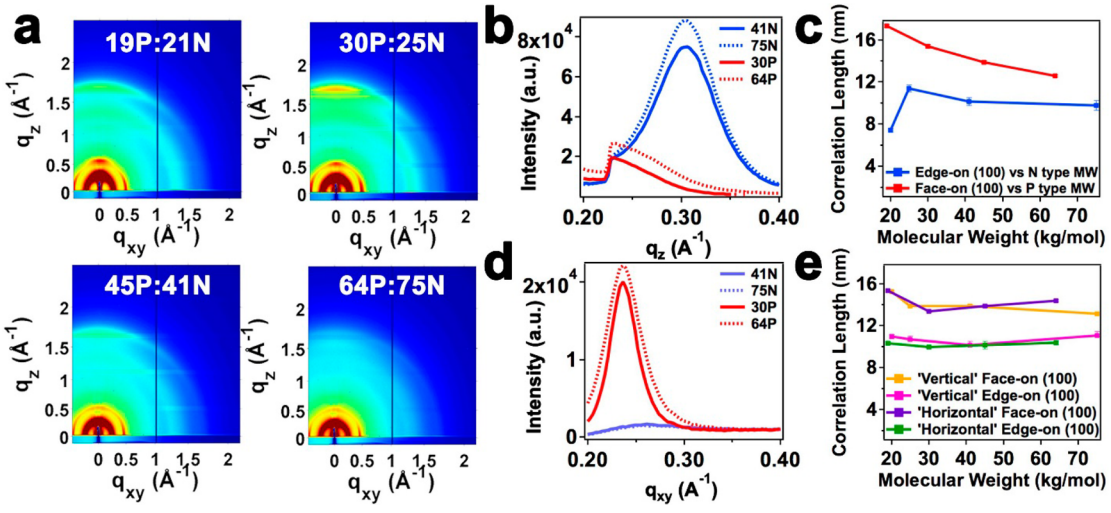

Figure 5. GIWAXS characteristics of APSC films. (a) 2D GIWAXS images of diagonal blends having the indicated M_ns. (b–e) (100) peak information from GIWAXS: (b) edge-on and (d) face-on (100) peaks of neat polymers. Correlation lengths of edge-on and face-on domains in (c) diagonal series **19P:21N**, **30P:25N**, **45P:41N**, and **64P:75N** blend films having the indicated M_ns and (e) horizontal and vertical series with **41N** held constant as the p-type M_n is varied and with **45P** held constant as the n-type M_n is varied.

DOI: 10.1021/jacs.5b10735
J. Am. Chem. Soc. 2016, 138, 1240–1251

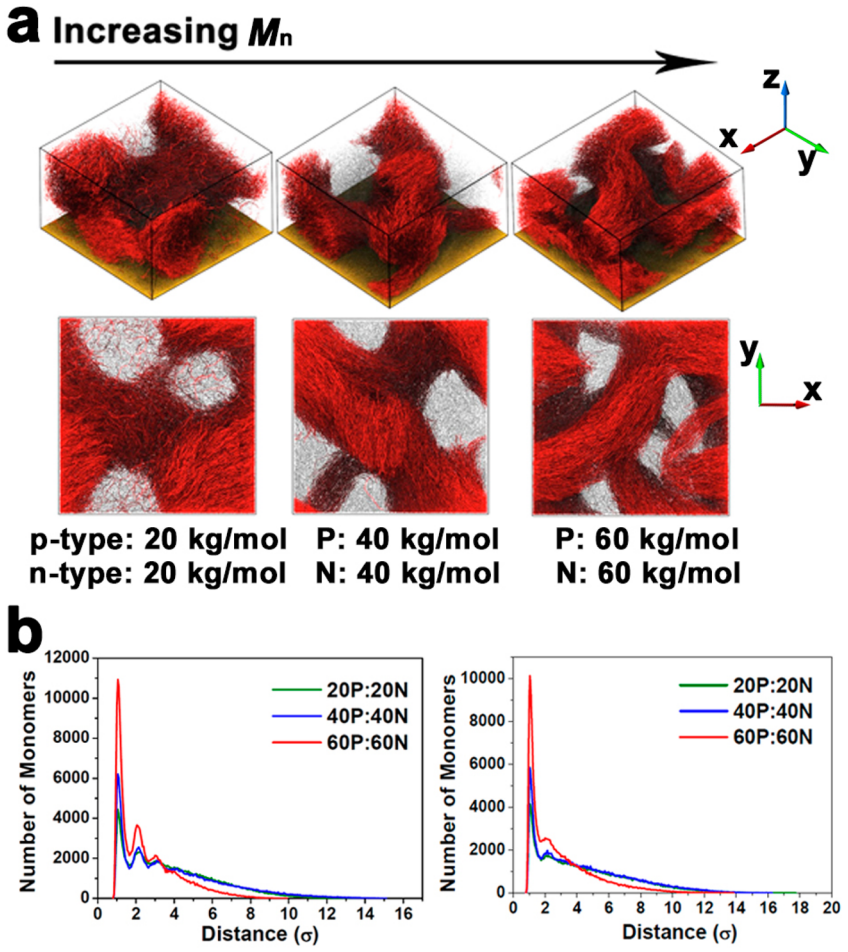

Figure 6. MD simulations of all-polymer blend morphology. (a) Polymer–polymer blend film morphology from coarse-grained MD simulations. The n-type polymer is represented by red beads and p-type polymer by gray beads. Snapshots were generated with the Visual Molecular Dynamics (VMD) package[82] and rendered with Tachyon ray-tracer.[83] (b) Left (right): Number of monomers of p (n) type at a certain distance from monomer of n (p) type averaged among all monomers of p (n) type. The distance between a monomer of p (n) type to its nearest neighboring monomer of type n (p) is measured.

combination (Figure 5c). The other two groups were selected by keeping either the **N2200** or **PTPD3T** M_n constant at the highest performance **41N** (horizontal case) or **45P** (vertical case), respectively, while varying M_n of the other component (Figure 5e).

Examining the blend lamellar (100) peaks reveals very little variation in d spacing (Figure S13, Table S8 in SI), which is expected since the stacking distance between molecules is more likely to be governed by side chains than by the number of repeat units (Figure 5a). However, examining correlation lengths in the diagonal case (Figure 5c), with increasing M_ns, reveals a contraction in domain size in the in-plane (100) domains dominated by **PTPD3T** and a more complicated trend for the **N2200**-dominated out-of-plane (100) domains, where the correlation length increases sharply from **19P:21N** to **30P:25N** and then declines. Interestingly, this trend in correlation lengths (Figure 5c) for different M_n combinations generally agrees with the DSC results discussed above, showing overall a decreasing crystallinity with higher M_n for both p- and n-type polymers. This argues that increasing M_n values lead to increased chain entanglement and result in reduced crystallinity through a disruption of the $\pi-\pi$ stacking interaction. However, when one of the polymers is held at a medium M_n, either at **45P** or **41N** as shown in Figure 5e, very little change in domain size in either the out-of-plane or the in-plane directions is observed as the other polymer M_n values are varied. This constant domain size when one of the polymers has medium M_n values indicates that the morphological properties of the two polymers are intertwined. Thus, even though the lower M_n neat polymers have larger ordered crystallites, they do not maintain their large domains in blends with the medium-M_n polymers. Therefore, optimum photovoltaic performance is achieved in blends of two medium-M_n polymers where the favorable characteristics of one are not compromised by morphological directing by the other component.

Collectively, the above TEM and GIWAXS data establish important trends in blend film morphology with varying polymer molecular weight. Clearly, increasing M_n of either **PTPD3T** or **N2200** reduces the degree of crystallinity, thereby resulting in more pronounced mixing of the two polymers. This result explains why higher M_ns promote higher device J_{sc} values due to the increased donor–acceptor interfacial area. The same effect increases recombination, which is responsible for the concomitant fall in *FF*.

Coarse-Grained Modeling of Polymer–Polymer Blend Film Morphology. Investigating polymer–polymer blend film morphology using a simplified physical model provides a different and complementary perspective, independent of the

DOI: 10.1021/jacs.5b10735
J. Am. Chem. Soc. 2016, 138, 1240–1251

experimental results, for better understanding of the physical processes that occur during blend film formation.[80,81] Here, considering that the phase separation feature sizes are a few tens of nanometers, which is prohibitively large in full atomistic simulations, large-scale molecular dynamics (MD) simulations were employed on a general coarse-grained model of blends of the two polymers. This model provides an excellent platform to analyze the morphological characteristics of the polymer−polymer blends. In this model, each monomer unit is coarse-grained into a single bead of size σ, connected via a bond potential, $U_{\text{bond}}(r) = \frac{1}{2}k_{\text{bond}}(r - r_0)^2$ and an angle potential, $U_{\text{angle}}(\theta) = \frac{1}{2}k_{\text{angle}}(\theta - \pi)^2$ to a nearby monomer unit. The bond rest length r_0 is arbitrarily set at 0.84σ to avoid bond crossings. Interactions for nonbonded beads are modeled by a shifted Lennard−Jones potential, which is written as $U_{\text{LJ}}(r_{ij}) = 4\epsilon\left[\left(\frac{\sigma}{r_{ij}}\right)^{12} - \left(\frac{\sigma}{r_{ij}}\right)^{6}\right] - U_{\text{LJ}}(r_{\text{cut}})$ for $r \leq r_{\text{cut}}$ ($r_{\text{cut}} = 3.0\sigma$) and $U_{\text{LJ}}(r_{ij}) = 0$ for $r > r_{\text{cut}}$. $\sigma \approx 1.6$ nm specifies the unit of length, and the Lennard−Jones potential wells for the description of monomer interactions are $\varepsilon_{\text{AA}} = 0.5\varepsilon_0$, $\varepsilon_{\text{AB}} = 0.3\varepsilon_0$, and $\varepsilon_{\text{BB}} = 0.1\varepsilon_0$, where $\varepsilon_0 \approx 0.38$ kcal mol^{-1} represents the unit of energy in our simulations. The condition of $\varepsilon_{\text{BB}} < \varepsilon_{\text{AB}}$ is used as $\varepsilon_{\text{BB}} > \varepsilon_{\text{AB}}$ will drive the polymer blend to phase separate. Constraints in $k_{\text{bond}} = 330\varepsilon_0$ and $k_{\text{angle}} = 20\varepsilon_0$ describe reasonable rigidity for such worm-like chains. An extra layer of fixed beads acting as a boundary condition for the bottom of the simulation box is included to model the film substrate. The model presented here can provide general insights into OPV polymer selection beyond the specific n- and p-type polymers employed in this work.

Figure 6a presents snapshots of simulated polymer−polymer blend film morphologies with varying p- and n-type polymer M_ns. From Figure 6a, using the lowest M_n combination, with both p- and n-type M_ns = 20 kg/mol (**20P:20N**), the simulated morphology shows highly rigid, short fibril-like structures, which leads to relatively large polymer domain sizes and small donor−acceptor interfaces. Increasing M_n (**40P:40N** blend) renders the polymers less crystalline, leading to a higher degree of miscibility with more intertwined polymer structures. Further increase in the length of both polymer chains to **60P:60N** with both M_ns = 60 kg/mol yields an even higher degree of miscibility and exhibiting a morphology with the most amorphous polymer features. These results are in excellent agreement with the experimental observations in Figure 4.

Finally, with the modeling results in hand, it is possible to extract physical constants of the morphology that can provide quantitative insights into the effect of molecular weight on morphology. Here, the nearest neighbor distance distribution is investigated (Figure 6b), which represents the distance between a monomer of p- (n-) type to its nearest neighboring monomer of n- (p-) type. Note that "dispersed polymers", which only account for 0−5% of the total polymer chains in the three simulated blend systems, are excluded from this calculation. Using this method, several important morphology features can be extracted mathematically from these plots. First, the height of the first peak at the distance 1.12 corresponds to the area of the donor−acceptor p/n interface or the interface-to-volume ratio as the volume is held constant. As an index of the exciton dissociation efficiency, higher p/n interface-to-volume ratios are desirable. Second, the maximum distance that the distribution reaches is relevant to the polymer bundle diameter. Ideally, uniform and medium-sized bundle networks contribute positively to high polymer conductivity. Lastly, a larger number of periodic peaks imply higher local polymer crystallinity. Thus, regions of the p-type polymer, the dominant polymer type, are highly ordered, while regions of the n-type polymer are relatively amorphous. On the basis of these results, the blend films composed of longer polymer chains are expected to have a higher interface-to-volume ratio and form fine bundle networks. Additionally, slower annealing would degrade the morphology and consequently the electrical conductivities.

Overall, the present coarse-grained model correctly predicts polymer−polymer blend morphologies that closely resemble the experimental observations. Most importantly, since this model does not target specific polymer structures, it can potentially be applied to a broad range of semicrystalline polymeric semiconductors, which represent promising candidates for all-polymer solar cells.

■ CONCLUSIONS

In this investigation of all-polymer OPVs, the effects of varying the number-average molecular weight (M_n) of both p-type **PTPD3T** and n-type **N2200** polymers on active layer photovoltaic performance, charge transport, and blend morphology are characterized. A straightforward and generalizable synthetic methodology to expeditiously access the required conjugated in-chain donor−acceptor polymers with controllable/predictable M_ns was developed based on the "extended" Carothers equation, and properties of the resulting p- and n-type polymers with varied M_ns were systematically investigated via a 4 × 4 all-polymer solar cell matrix of donor and acceptor polymers. It is found that increasing the M_n values of both the p- and the n-type component polymers simultaneously transforms the polymer domains in the low-M_n polymer−polymer blends from relatively ordered and highly crystalline, with largely phase-separated features, into relatively disordered, amorphous, and miscible structures in the high-M_n blends. Consistent with the morphology characteristics, the all-polymer solar cell performance exhibits a steady increase in J_{sc} but a reduction in *FF* with increasing polymer M_n. The J_{sc} enhancement is explained by increased interfacial area between the donor and the acceptor polymers, resulting in enhanced exciton dissociation, while the random, disordered blend morphology contributes to a high degree of recombination and lower *FF*. As a result, the highest PCEs are achieved for devices based on intermediary molecular weight for both polymers, where the opposing charge generation and transport processes become well balanced. The above findings are further supported by charge transport measurements and coarse-grained modeling results. Note that the optimal devices exhibit PCEs that are increased up to 2-fold versus devices based on polymers with nonoptimal M_ns. The present work highlights the importance of molecular weight tuning of *both* polymer components and establishes a promising strategy and relevant synthetic tools for optimizing future efficiencies of all-polymer solar cells. We anticipate that further PCE increases for many all-polymer solar cells can be achieved by utilizing the present polymer molecular weight optimization matrix approach, thereby advancing toward practical photovoltaic technologies.

■ EXPERIMENTAL SECTION

Materials Synthesis. All materials were synthesized and characterized according to modified literature procedures. The details

DOI: 10.1021/jacs.5b10735
J. Am. Chem. Soc. 2016, 138, 1240−1251

of the synthesis and characterization are provided in the Supporting Information.

APSC Device Fabrication and Characterization. Prepatterned indium tin oxide (ITO)-coated glass wafers (Thin Film Devices, Inc.) with a thickness of ∼280 nm and sheet resistance of ∼10 Ω/sq were used as substrates. ITO electrodes were cleaned by sequential sonication in hexane, deionized (DI) water, methanol, isopropanol, and acetone and finally UV/ozone treatment (Jelight Co.) for 30 min. The cathode interfacial layer, ZnO, was deposited from a precursor solution prepared from 0.5 M zinc acetate dehydrate in 0.5 M monoethanolamine and 2-methoxy ethanol, spun cast at 5000 rpm for 30 s, and annealed at 170 °C. For optimal performance, active layer solutions were prepared with 1:1 **PTPD3T**:**N2200** weight ratios in chloroform:1-chloronaphthalene (99:1 v/v) at a **PTPD3T** concentration ∼3−5 mg mL^{-1}. Chloronaphthalene was used as a solvent additive to disrupt the self-aggregation tendency of N2200.[39] Active layer solutions were spin coated in an N_2-filled glovebox at 3000−6000 rpm to obtain a thickness of 70 nm. Thin layers of 7.5 nm MoO_3 and 120 nm of Ag were then thermally evaporated through a shadow mask at ∼10^{-6} Torr. Device I−V characteristics were measured under AM1.5G light (100 mW cm^{-2}) using the Xe arc lamp of a Spectra-Nova Class A solar simulator. The light intensity was calibrated using an NREL-certified monocrystalline Si diode coupled to a KG3 filter to bring the spectral mismatch to unity. Four-point contact measurements were performed, and electrical characterizations were measured with a Keithley 2400 unit. The area of all devices was 6 mm^2, and a 6 mm^2 aperture was used on top of cells during measurements. EQEs were acquired using an Oriel model QE-PV-SI instrument equipped with a NIST-certified Si diode. Monochromatic light was generated with an Oriel 300 W lamp source.

SCLC Mobility Measurements. Hole-only diodes were fabricated on ITO-coated glass with a PEDOT:PSS bottom contact and a MoO_3/Au top contact, whereas electron-only diodes were fabricated on ITO-coated glass with a ZnO bottom contact and a Cs_2CO_3/Al (1 nm/100 nm) top contact. The top contact was the injecting electrode in both cases. The semiconducting layer was either neat polymer or polymer blend (as used in the optimal solar cell devices). Device areas (A) were 200 × 200 μm^2.

TEM. TEM measurements were performed with a JEOL JEM-2100F instrument, with samples prepared directly from films prepared under identical conditions as actual devices on PEDOT:PSS. The substrates were immersed in DI water, and the floated active layer thin films are subsequently transferred to a lacey carbon TEM grid (Ted Pella, inc.)

GIWAXS. GIWAXS measurements were performed at Beamline 8ID-E at the Advanced Photon Source at Argonne National Laboratory. The sample was irradiated at an incidence angle of 0.18° in air at 7.35 keV for 5 summed exposures of 5 s (totaling 25 s of exposure), and the scattering was recorded on a Pilatus 1 M detector located 204 mm from the sample. The background was subtracted by fitting the curves to an exponential decay, and peaks were fit using a multipeak Gaussian fitting program in Igor Pro. The correlation length was calculated using a modified Scherrer analysis which accounts for instrument resolution using the standard shape factor (K) = 0.866 for lamellar polymer aggregates. The (100) peak was fit to determine the lamellar correlation length. The correlation length for the π-stacking (010) peak was not calculated due to the overlap of **PTPD3T** and **N2200** π-stacking peaks. All correlation lengths are a minimum value since they do not account for broadening of the peaks due to crystalline disorder.

Coarse-Grained Simulation. With the current model, molecular dynamics simulations were performed on the HOOMD-blue package[83,84] in the constant pressure and temperature ensemble (NPT) with the temperature controlled via the Nosé−Hoover thermostat.[85,86] Simulations are performed with periodic boundary conditions in the x and y directions with constant pressure set at P = 1.0. Note that periodicity in the z direction is unnecessary due to the layer of substrate beads. During the simulation, the system is first heated to T = 5.0 for 5 × 10^5 time steps (each time step equals to 0.28 ps) to randomize the polymer blend. Then the blend is annealed and stabilized at T = 1.9, followed by a quick annealing process from T = 1.9 to T = 1.55 during 2.6 × 10^6 time steps. Holding the pressure constant, the simulation box is allowed to shrink in the z direction during the annealing from ∼110 to ∼90 nm. Systems sized at 160 nm × 160 nm on x−y dimension were studied, each composed of 466 000 monomers. A typical simulation of such a large scale system takes about 2 days on a single Tesla K40m graphic card.

■ ASSOCIATED CONTENT

Supporting Information

The Supporting Information is available free of charge on the ACS Publications website at DOI: 10.1021/jacs.5b10735.

Synthesis and characterization of monomers and polymers, NMR, UV−vis, CV, UPS, and DSC spectra, SCLC and GIWAXS measurements (PDF)

■ AUTHOR INFORMATION

Corresponding Authors

*l-chen@northwestern.edu
*r-chang@northwestern.edu
*a-facchetti@northwestern.edu
*m-olvera@northwestern.edu
*t-marks@northwestern.edu

Author Contributions

The manuscript was written through contributions of all authors. All authors have given approval to the final version of the manuscript.

Notes

The authors declare no competing financial interest.

■ ACKNOWLEDGMENTS

This research was supported in part by Argonne-Northwestern Solar Energy Research (ANSER) Center, an Energy Frontier Research Center funded by the U.S. Department of Energy, Office of Science, Office of Basic Energy Sciences under Award Number DE-SC0001059, by the U.S. Department of Energy, Office of Science, and Office of Basic Energy Sciences under Award Number DE-FG02-08ER46536, AFOSR grant FA9550-15-1-0044, and the Northwestern University Materials Research Science and Engineering Center under NSF grant DMR-1121262. T.I.N.G.L. and M.O.C. were supported by award 70NANB14H012 from the U.S. Department of Commerce, National Institute of Standards and Technology as part of the Center for Hierarchical Materials Design (CHiMaD). A.S.D. thanks the Camille and Henry Dreyfus Postdoctoral Program in Environmental Chemistry for a fellowship, and T.J.A. thanks the NSF for a predoctoral fellowship. We thank the Integrated Molecular Structure Education and Research Center (IMSERC) for characterization facilities supported by Northwestern University, National Science Foundation (NSF) under NSF CHE-0923236 and CHE-9871268 (1998), Pfizer, and the State of Illinois. Use of the Advanced Photon Source, an Office of Science User Facility operated for the U.S. Department of Energy (DOE) Office of Science by Argonne National Laboratory, was supported by the U.S. DOE under Contract No. DE-AC02-06CH11357.

■ REFERENCES

(1) Liang, Y.; Xu, Z.; Xia, J.; Tsai, S.-T.; Wu, Y.; Li, G.; Ray, C.; Yu, L. *Adv. Mater.* **2010**, *22*, E135.
(2) Li, W.; Hendriks, K. H.; Roelofs, W. S. C.; Kim, Y.; Wienk, M. M.; Janssen, R. A. J. *Adv. Mater.* **2013**, *25*, 3182.

DOI: 10.1021/jacs.5b10735
J. Am. Chem. Soc. 2016, 138, 1240−1251

(3) Liu, Y.; Zhao, J.; Li, Z.; Mu, C.; Ma, W.; Hu, H.; Jiang, K.; Lin, H.; Ade, H.; Yan, H. *Nat. Commun.* **2014**, *5*, 5293.
(4) Nguyen, T. L.; Choi, H.; Ko, S. J.; Uddin, M. A.; Walker, B.; Yum, S.; Jeong, J. E.; Yun, M. H.; Shin, T. J.; Hwang, S.; Kim, J. Y.; Woo, H. Y. *Energy Environ. Sci.* **2014**, *7*, 3040.
(5) Zhang, M.; Guo, X.; Ma, W.; Ade, H.; Hou, J. *Adv. Mater.* **2014**, *26*, 5880.
(6) Guo, X.; Zhou, N.; Lou, S. J.; Smith, J.; Tice, D. B.; Hennek, J. W.; Ortiz, R. P.; Navarrete, J. T. L.; Li, S.; Strzalka, J.; Chen, L. X.; Chang, R. P. H.; Facchetti, A.; Marks, T. J. *Nat. Photonics* **2013**, *7*, 825.
(7) Dou, L.; Chen, C.-C.; Yoshimura, K.; Ohya, K.; Chang, W.-H.; Gao, J.; Liu, Y.; Richard, E.; Yang, Y. *Macromolecules* **2013**, *46*, 3384.
(8) Chen, J.-D.; Cui, C.; Li, Y.-Q.; Zhou, L.; Ou, Q.-D.; Li, C.; Li, Y.; Tang, J.-X. *Adv. Mater.* **2015**, *27*, 1035.
(9) Earmme, T.; Hwang, Y.-J.; Murari, N. M.; Subramaniyan, S.; Jenekhe, S. A. *J. Am. Chem. Soc.* **2013**, *135*, 14960.
(10) Zang, Y.; Li, C.-Z.; Chueh, C.-C.; Williams, S. T.; Jiang, W.; Wang, Z.-H.; Yu, J.-S.; Jen, A. K. Y. *Adv. Mater.* **2014**, *26*, 5708.
(11) Mori, D.; Benten, H.; Okada, I.; Ohkita, H.; Ito, S. *Energy Environ. Sci.* **2014**, *7*, 2939.
(12) Earmme, T.; Hwang, Y.-J.; Subramaniyan, S.; Jenekhe, S. A. *Adv. Mater.* **2014**, *26*, 6080.
(13) Mu, C.; Liu, P.; Ma, W.; Jiang, K.; Zhao, J.; Zhang, K.; Chen, Z.; Wei, Z.; Yi, Y.; Wang, J.; Yang, S.; Huang, F.; Facchetti, A.; Ade, H.; Yan, H. *Adv. Mater.* **2014**, *26*, 7224.
(14) Lin, Y.; Zhang, Z.-G.; Bai, H.; Wang, J.; Yao, Y.; Li, Y.; Zhu, D.; Zhan, X. *Energy Environ. Sci.* **2015**, *8*, 610.
(15) Kang, H.; Uddin, M. A.; Lee, C.; Kim, K.-H.; Nguyen, T. L.; Lee, W.; Li, Y.; Wang, C.; Woo, H. Y.; Kim, B. J. *J. Am. Chem. Soc.* **2015**, *137*, 2359.
(16) Jung, J. W.; Jo, J. W.; Chueh, C.-C.; Liu, F.; Jo, W. H.; Russell, T. P.; Jen, A. K. Y. *Adv. Mater.* **2015**, *27*, 3310.
(17) Yuan, M.; Durban, M. M.; Kazarinoff, P. D.; Zeigler, D. F.; Rice, A. H.; Segawa, Y.; Luscombe, C. K. *J. Polym. Sci., Part A: Polym. Chem.* **2013**, *51*, 4061.
(18) Durban, M. M.; Kazarinoff, P. D.; Segawa, Y.; Luscombe, C. K. *Macromolecules* **2011**, *44*, 4721.
(19) Chiechi, R. C.; Havenith, R. W. A.; Hummelen, J. C.; Koster, L. J. A.; Loi, M. A. *Mater. Today* **2013**, *16*, 281.
(20) Zhou, N. J.; Lin, H.; Lou, S. J.; Yu, X. G.; Guo, P. J.; Manley, E. F.; Loser, S.; Hartnett, P.; Huang, H.; Wasielewski, M. R.; Chen, L. X.; Chang, R. P. H.; Facchetti, A.; Marks, T. J. *Adv. Energy Mater.* **2014**, *4*, 8.
(21) Li, C.; Wonneberger, H. *Adv. Mater.* **2012**, *24*, 613.
(22) Jung, I. H.; Lo, W.-Y.; Jang, J.; Chen, W.; Zhao, D.; Landry, E. S.; Lu, L.; Talapin, D. V.; Yu, L. *Chem. Mater.* **2014**, *26*, 3450.
(23) Jung, I. H.; Zhao, D.; Jang, J.; Chen, W.; Landry, E. S.; Lu, L.; Talapin, D. V.; Yu, L. *Chem. Mater.* **2015**, *27*, 5941.
(24) Bisri, S. Z.; Piliego, C.; Gao, J.; Loi, M. A. *Adv. Mater.* **2014**, *26*, 1176.
(25) Fabiano, S.; Wang, H.; Piliego, C.; Jaye, C.; Fischer, D. A.; Chen, Z.; Pignataro, B.; Facchetti, A.; Loo, Y.-L.; Loi, M. A. *Adv. Funct. Mater.* **2011**, *21*, 4479.
(26) Piliego, C.; Jarzab, D.; Gigli, G.; Chen, Z.; Facchetti, A.; Loi, M. A. *Adv. Mater.* **2009**, *21*, 1573.
(27) Hwang, Y.-J.; Earmme, T.; Courtright, B. A. E.; Eberle, F. N.; Jenekhe, S. A. *J. Am. Chem. Soc.* **2015**, *137*, 4424.
(28) Li, H.; Hwang, Y.-J.; Courtright, B. A. E.; Eberle, F. N.; Subramaniyan, S.; Jenekhe, S. A. *Adv. Mater.* **2015**, *27*, 3266.
(29) Facchetti, A. *Mater. Today* **2013**, *16*, 123.
(30) Salleo, A.; Kline, R. J.; DeLongchamp, D. M.; Chabinyc, M. L. *Adv. Mater.* **2010**, *22*, 3812.
(31) Noriega, R.; Rivnay, J.; Vandewal, K.; Koch, F. P. V.; Stingelin, N.; Smith, P.; Toney, M. F.; Salleo, A. *Nat. Mater.* **2013**, *12*, 1038.
(32) Spano, F. C.; Silva, C. *Annu. Rev. Phys. Chem.* **2014**, *65*, 477.
(33) Noriega, R.; Rivnay, J.; Vandewal, K.; Koch, F. P. V.; Stingelin, N.; Smith, P.; Toney, M. F.; Salleo, A. *Nat. Mater.* **2013**, *12*, 1038.
(34) Liu, C.; Wang, K.; Hu, X.; Yang, Y.; Hsu, C.-H.; Zhang, W.; Xiao, S.; Gong, X.; Cao, Y. *ACS Appl. Mater. Interfaces* **2013**, *5*, 12163.
(35) Bartelt, J. A.; Douglas, J. D.; Mateker, W. R.; Labban, A. E.; Tassone, C. J.; Toney, M. F.; Fréchet, J. M. J.; Beaujuge, P. M.; McGehee, M. D. *Adv. Energy Mater.* **2014**, *4*, n/a.
(36) Veenstra, S. C.; Loos, J.; Kroon, J. M. *Prog. Photovoltaics* **2007**, *15*, 727.
(37) Menczel, J. D.; Judovits, L.; Prime, R. B.; Bair, H. E.; Reading, M.; Swier, S. *Thermal Analysis of Polymers*; John Wiley & Sons, Inc.: New York, 2008; p 7.
(38) Zhou, N.; Buchholz, D. B.; Zhu, G.; Yu, X.; Lin, H.; Facchetti, A.; Marks, T. J.; Chang, R. P. H. *Adv. Mater.* **2014**, *26*, 1098.
(39) Schubert, M.; Dolfen, D.; Frisch, J.; Roland, S.; Steyrleuthner, R.; Stiller, B.; Chen, Z. H.; Scherf, U.; Koch, N.; Facchetti, A.; Neher, D. *Adv. Energy Mater.* **2012**, *2*, 369.
(40) Podzorov, V. *Nat. Mater.* **2013**, *12*, 947.
(41) Hwang, Y.-J.; Courtright, B. A. E.; Ferreira, A. S.; Tolbert, S. H.; Jenekhe, S. A. *Adv. Mater.* **2015**, *27*, 4578.
(42) Meager, I.; Ashraf, R. S.; Nielsen, C. B.; Donaghey, J. E.; Huang, Z.; Bronstein, H.; Durrant, J. R.; McCulloch, I. *J. Mater. Chem. C* **2014**, *2*, 8593.
(43) Subbiah, J.; Purushothaman, B.; Chen, M.; Qin, T.; Gao, M.; Vak, D.; Scholes, F. H.; Chen, X.; Watkins, S. E.; Wilson, G. J.; Holmes, A. B.; Wong, W. W. H.; Jones, D. J. *Adv. Mater.* **2015**, *27*, 702.
(44) Xiao, Z.; Sun, K.; Subbiah, J.; Qin, T.; Lu, S.; Purushothaman, B.; Jones, D. J.; Holmes, A. B.; Wong, W. W. H. *Polym. Chem.* **2015**, *6*, 2312.
(45) Kingsley, J. W.; Marchisio, P. P.; Yi, H.; Iraqi, A.; Kinane, C. J.; Langridge, S.; Thompson, R. L.; Cadby, A. J.; Pearson, A. J.; Lidzey, D. G.; Jones, R. A. L.; Parnell, A. J. *Sci. Rep.* **2014**, *4*, 5286.
(46) Chu, T.-Y.; Lu, J.; Beaupré, S.; Zhang, Y.; Pouliot, J.-R.; Zhou, J.; Najari, A.; Leclerc, M.; Tao, Y. *Adv. Funct. Mater.* **2012**, *22*, 2345.
(47) Osaka, I.; Saito, M.; Mori, H.; Koganezawa, T.; Takimiya, K. *Adv. Mater.* **2012**, *24*, 425.
(48) Coffin, R. C.; Peet, J.; Rogers, J.; Bazan, G. C. *Nat. Chem.* **2009**, *1*, 657.
(49) Müller, C.; Wang, E.; Andersson, L. M.; Tvingstedt, K.; Zhou, Y.; Andersson, M. R.; Inganäs, O. *Adv. Funct. Mater.* **2010**, *20*, 2124.
(50) Gibson, G. L.; Gao, D.; Jahnke, A. A.; Sun, J.; Tilley, A. J.; Seferos, D. S. *J. Mater. Chem. A* **2014**, *2*, 14468.
(51) Harschneck, T.; Zhou, N.; Manley, E. F.; Lou, S. J.; Yu, X.; Butler, M. R.; Timalsina, A.; Turrisi, R.; Ratner, M. A.; Chen, L. X.; Marks, T. J. *Chem. Commun.* **2014**, *50*, 9609.
(52) Li, W.; Yang, L.; Tumbleston, J. R.; Yan, L.; Ade, H.; You, W. *Adv. Mater.* **2014**, *26*, 4456.
(53) Stille, J. K. *Angew. Chem., Int. Ed. Engl.* **1986**, *25*, 508.
(54) Carsten, B.; He, F.; Son, H. J.; Xu, T.; Yu, L. *Chem. Rev.* **2011**, *111*, 1493.
(55) Odian, G. *Principles of Polymerization*; John Wiley & Sons, Inc.: New York, 2004; p 198.
(56) Karpov, Y.; Zhao, W.; Raguzin, I.; Beryozkina, T.; Bakulev, V.; Al-Hussein, M.; Häußler, L.; Stamm, M.; Voit, B.; Facchetti, A.; Tkachov, R.; Kiriy, A. *ACS Appl. Mater. Interfaces* **2015**, *7*, 12478.
(57) Steyrleuthner, R.; Schubert, M.; Howard, I.; Klaumünzer, B.; Schilling, K.; Chen, Z.; Saalfrank, P.; Laquai, F.; Facchetti, A.; Neher, D. *J. Am. Chem. Soc.* **2012**, *134*, 18303.
(58) Steyrleuthner, R.; Di Pietro, R.; Collins, B. A.; Polzer, F.; Himmelberger, S.; Schubert, M.; Chen, Z.; Zhang, S.; Salleo, A.; Ade, H.; Facchetti, A.; Neher, D. *J. Am. Chem. Soc.* **2014**, *136*, 4245.
(59) Yan, H.; Chen, Z.; Zheng, Y.; Newman, C.; Quinn, J. R.; Dotz, F.; Kastler, M.; Facchetti, A. *Nature* **2009**, *457*, 679.
(60) Guo, X.; Zhou, N.; Lou, S. J.; Hennek, J. W.; Ponce Ortiz, R.; Butler, M. R.; Boudreault, P.-L. T.; Strzalka, J.; Morin, P.-O.; Leclerc, M.; López Navarrete, J. T.; Ratner, M. A.; Chen, L. X.; Chang, R. P. H.; Facchetti, A.; Marks, T. J. *J. Am. Chem. Soc.* **2012**, *134*, 18427.
(61) Zhou, N.; Guo, X.; Ortiz, R. P.; Li, S.; Zhang, S.; Chang, R. P. H.; Facchetti, A.; Marks, T. J. *Adv. Mater.* **2012**, *24*, 2242.
(62) Gibson, G. L.; Gao, D.; Jahnke, A. A.; Sun, J.; Tilley, A. J.; Seferos, D. S. *J. Mater. Chem. A* **2014**, *2*, 14468.

DOI: 10.1021/jacs.5b10735
J. Am. Chem. Soc. 2016, 138, 1240−1251

(63) Halkyard, C. E.; Rampey, M. E.; Kloppenburg, L.; Studer-Martinez, S. L.; Bunz, U. H. F. *Macromolecules* **1998**, *31*, 8655.
(64) Kim, J.; Swager, T. M. *Nature* **2001**, *411*, 1030.
(65) Scharber, M. C.; Mühlbacher, D.; Koppe, M.; Denk, P.; Waldauf, C.; Heeger, A. J.; Brabec, C. J. *Adv. Mater.* **2006**, *18*, 789.
(66) Ameri, T.; Dennler, G.; Lungenschmied, C.; Brabec, C. J. *Energy Environ. Sci.* **2009**, *2*, 347.
(67) Djurovich, P. I.; Mayo, E. I.; Forrest, S. R.; Thompson, M. E. *Org. Electron.* **2009**, *10*, 515.
(68) D'Andrade, B. W.; Datta, S.; Forrest, S. R.; Djurovich, P.; Polikarpov, E.; Thompson, M. E. *Org. Electron.* **2005**, *6*, 11.
(69) McCulloch, I.; Heeney, M.; Chabinyc, M. L.; DeLongchamp, D.; Kline, R. J.; Cölle, M.; Duffy, W.; Fischer, D.; Gundlach, D.; Hamadani, B.; Hamilton, R.; Richter, L.; Salleo, A.; Shkunov, M.; Sparrowe, D.; Tierney, S.; Zhang, W. *Adv. Mater.* **2009**, *21*, 1091.
(70) Liu, F.; Chen, D.; Wang, C.; Luo, K.; Gu, W.; Briseno, A. L.; Hsu, J. W. P.; Russell, T. P. *ACS Appl. Mater. Interfaces* **2014**, *6*, 19876.
(71) Zen, A.; Saphiannikova, M.; Neher, D.; Grenzer, J.; Grigorian, S.; Pietsch, U.; Asawapirom, U.; Janietz, S.; Scherf, U.; Lieberwirth, I.; Wegner, G. *Macromolecules* **2006**, *39*, 2162.
(72) Huang, H.; Zhou, N.; Ortiz, R. P.; Chen, Z.; Loser, S.; Zhang, S.; Guo, X.; Casado, J.; López Navarrete, J. T.; Yu, X.; Facchetti, A.; Marks, T. J. *Adv. Funct. Mater.* **2014**, *24*, 2782.
(73) Mandoc, M. M.; Veurman, W.; Koster, L. J. A.; de Boer, B.; Blom, P. W. M. *Adv. Funct. Mater.* **2007**, *17*, 2167.
(74) McNeill, C. R.; Halls, J. J. M.; Wilson, R.; Whiting, G. L.; Berkebile, S.; Ramsey, M. G.; Friend, R. H.; Greenham, N. C. *Adv. Funct. Mater.* **2008**, *18*, 2309.
(75) Fabiano, S.; Himmelberger, S.; Drees, M.; Chen, Z. H.; Altamimi, R. M.; Salleo, A.; Loi, M. A.; Facchetti, A. *Adv. Energy Mater.* **2014**, *4*, 7.
(76) Bartesaghi, D.; Perez, I. d. C.; Kniepert, J.; Roland, S.; Turbiez, M.; Neher, D.; Koster, L. J. A. *Nat. Commun.* **2015**, *6*, 7083.
(77) Peet, J.; Kim, J. Y.; Coates, N. E.; Ma, W. L.; Moses, D.; Heeger, A. J.; Bazan, G. C. *Nat. Mater.* **2007**, *6*, 497.
(78) Peet, J.; Heeger, A. J.; Bazan, G. C. *Acc. Chem. Res.* **2009**, *42*, 1700.
(79) Smilgies, D.-M. *J. Appl. Crystallogr.* **2009**, *42*, 1030.
(80) Sumpter, B. G.; Meunier, V. *J. Polym. Sci., Part B: Polym. Phys.* **2012**, *50*, 1071.
(81) Lee, C.-K.; Pao, C.-W.; Chu, C.-W. *Energy Environ. Sci.* **2011**, *4*, 4124.
(82) Humphrey, W.; Dalke, A.; Schulten, K. *J. Mol. Graphics* **1996**, *14*, 33.
(83) Glaser, J.; Nguyen, T. D.; Anderson, J. A.; Lui, P.; Spiga, F.; Millan, J. A.; Morse, D. C.; Glotzer, S. C. *Comput. Phys. Commun.* **2015**, *192*, 97.
(84) Anderson, J. A.; Lorenz, C. D.; Travesset, A. *J. Comput. Phys.* **2008**, *227*, 5342.
(85) Nose, S. *Mol. Phys.* **1984**, *52*, 255.
(86) Hoover, W. G. *Phys. Rev. A: At., Mol., Opt. Phys.* **1985**, *31*, 1695.

DOI: 10.1021/jacs.5b10735
J. Am. Chem. Soc. 2016, 138, 1240−1251